ACS APPLIED MATERIALS & INTERFACES
Research Article
www.acsami.org

Mesoporous Titania Microspheres with Highly Tunable Pores as an Anode Material for Lithium Ion Batteries

Michael G. Fischer,[†] Xiao Hua,*[,†] Bodo D. Wilts,[†] Ilja Gunkel,[†] Thomas M. Bennett,[‡] and Ullrich Steiner*[,†]

[†]Adolphe Merkle Institute, Université de Fribourg, Chemin des Verdiers 4, 1700 Fribourg, Switzerland
[‡]School of Chemistry, University of Nottingham, University Park, Nottingham NG7 2RD, United Kingdom

Supporting Information

ABSTRACT: Mesoporous titania microspheres (MTMs) have been employed in many applications, including (photo)catalysis as well as energy conversion and storage. Their morphology offers a hierarchical structural design motif that lends itself to being incorporated into established large-scale fabrication processes. Despite the fact that device performance hinges on the precise morphological characteristics of these materials, control over the detailed mesopore structure and the tunability of the pore size remains a challenge. Especially the accessibility of a wide range of mesopore sizes by the same synthesis method is desirable, as this would allow for a comparative study of the relationship between structural features and performance. Here, we report a method that combines sol−gel chemistry with polymer micro- and macrophase separation to synthesize porous titania spheres with diameters in the micrometer range. The as-prepared MTMs exhibit well-defined, accessible porosities with mesopore sizes adjustable by the choice of the polymers. When applied as an anode material in lithium ion batteries (LIBs), the MTMs demonstrate excellent performance. The influence of the pore size and an in situ carbon coating on charge transport and storage is examined, providing important insights for the optimization of structured titania anodes in LIBs. Our synthesis strategy presents a facile one-pot approach that can be applied to different structure-directing agents and inorganic materials, thus further extending its scope of application.

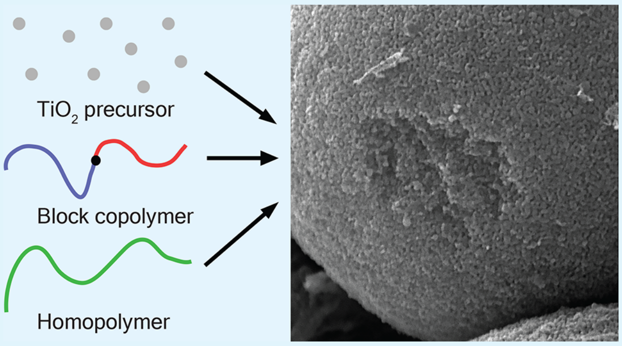

KEYWORDS: *self-assembly, sol−gel, block copolymer, titania, microspheres, battery, hierarchical*

1. INTRODUCTION

Titanium dioxide is an energy material which is used in catalysis,[1,2] solar cells,[3−6] and energy storage.[7−13] These applications benefit from elaborate titania nanostructures that offer very high surface areas in conjunction with good electron and possibly ion transport properties. Standard lithium ion battery (LIB) electrodes employ micrometer-sized particles and excel in terms of structural stability and electronic conductivity, at the expense of ionic transport. Nanomaterials provide large surface areas for charge-transfer processes and reduced diffusion lengths for lithium ions in the active material.[14] Electrodes comprising nanoparticles are advantageous for these reasons, but they suffer from low volumetric energy densities and difficulties in maintaining interparticle contact. A combination of these two concepts may therefore be advantageous, the synthesis of micrometer-sized particles featuring an internal nanostructure, simultaneously circumventing the disadvantages of micro- and nanoparticles.[15] Additionally, electrodes composed of mesoporous (micro)particles possess hierarchical features which can be exploited to further enhance device performance.[16]

Following this idea, mesocrystals assembled from agglomerated titania nanoparticles[17−19] and nanosized titania cubes[20] have been studied as anode materials, revealing the significance their nanostructure has on the electrochemical performance. Porous monodisperse microspheres with different pore sizes have been synthesized[21] and applied in LIBs, with the smallest studied pore size (15 nm) showing the highest rate capabilities.[12] Similarly, spheres composed of anatase nanosheets,[22] hollow multishelled spheres,[23] and hollow microspheres with a mesoporous carbon-coated shell[24] have demonstrated excellent rate performances. Besides lithium ion technologies, mesoporous carbon-coated titania spheres[11] and nanoparticles[13] have been identified as promising candidates for anodes in sodium ion batteries. Hierarchical TiO_2 spheres have also been used as host material for lithium−sulfur batteries.[25]

Among these examples, mesoporous titania microspheres (MTMs) with controllable pores and sphere dimensions stand out since they offer a structural hierarchy with large internal surface area and a well-defined shape on the micrometer scale that allows for high packing densities.[12] Numerous synthesis

Received: March 5, 2017
Accepted: June 13, 2017
Published: June 13, 2017

DOI: 10.1021/acsami.7b03155
ACS Appl. Mater. Interfaces 2017, 9, 22388−22397

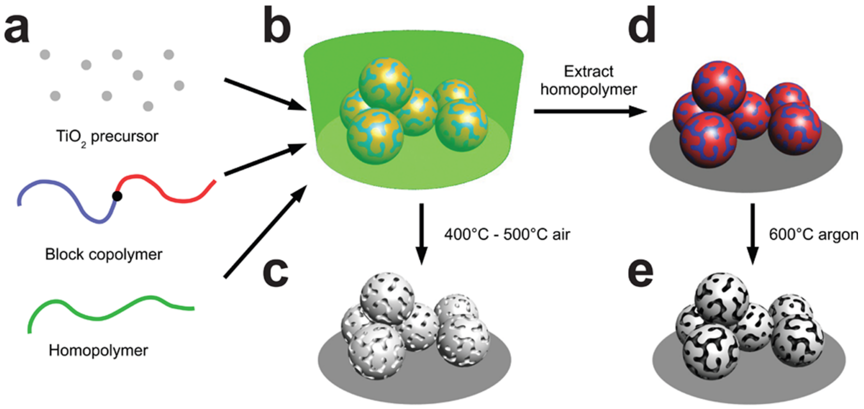

Figure 1. Schematic of the self-assembly process forming MTMs. (a) The titania precursor is mixed with a BCP and a homopolymer in a solvent. (b) Upon solvent evaporation, the homopolymer macrophase separates from the titania/BCP composite, resulting in a microspherical structure. The TiO_2 precursors are confined within the hydrophilic part of the BCP. (c) When calcined in air, the titania crystallizes, whereas the BCP is burned off, resulting in a mesoporous structure. (d) Alternatively, the homopolymer can be extracted from the composite. (e) Subsequent annealing under an inert atmosphere crystallizes the titania and carbonizes the BCP, forming carbon-coated mesopores.

methods have been developed to fabricate porous microspheres,[26] including spray-drying,[2] infiltration of preformed structures,[27] sol−gel processes,[1,6,8,13,21,28,29] and hydrothermal/solvothermal methods,[4,7,9−11,21,22,29,30] or combinations thereof. Some methods involve the use of a templating agent to create the mesopores,[1,2,4,6,7,13,27−30] whereas others rely on chemical reactions and processing conditions to create a mesostructure.[8−11,22,31] Full structural control over the mesopores and the sphere dimensions however still remains a challenge.

An approach that generates well-defined morphologies on the mesoscale uses block copolymer (BCP) self-assembly. By combining sol−gel chemistry with the microphase-separated structure of BCPs, mesostructured inorganic materials, including titania, have been synthesized.[32,33] This concept of using BCPs as soft templates has been utilized to fabricate mesoporous films with different pore sizes,[34] ordered carbon-coated mesoporous TiO_2,[35] hierarchically porous materials,[16] and mesostructured particles.[29] While ordered titania structures replicated from hard templates have also been realized,[36] their fabrication requires multiple complicated steps. Related titanium-based materials, such as $Li_4Ti_5O_{12}$[37] and $TiNb_2O_7$[38] also benefit from BCP templating when employed in LIBs. It remains however difficult to incorporate BCP-templated inorganic materials into microspheres. Meanwhile, there has been considerable success in fabricating polymeric particles with well-defined internal morphologies based on BCP self-assembly within droplets.[27,39−42] These structures are typically fabricated by an emulsion or solvent exchange method. A postprocessing step is thus required to load one of the polymeric components with an inorganic material, possibly leading to structural changes.[27]

In this paper, we demonstrate a facile one-pot method to synthesize MTMs. It combines sol−gel chemistry with BCP microphase separation to form a mesostructure with adjustable pore size. Macrophase separation with a suitable homopolymer confines this structure into microspheres. We show that precise control over the mesopore size can be achieved by using BCPs of different molecular weights and compositions. Upon heat treatment, the initially amorphous material crystallizes to form anatase, a titania polymorph that has been widely investigated as an anode material for LIBs. In particular, there is growing interest in nanostructured anatase due to its size-dependent kinetic and thermodynamic behavior upon lithium insertion.[14] Moreover, the BCP scaffold can be carbonized in situ, forming a conductive coating on the mesopores.[35,43] The ability to adjust these morphological characteristics allowed us to study their impact on the lithiation kinetics and charge storage mechanisms. This identifies design criteria that will help to systematically optimize specific properties of titania anodes.

2. RESULTS AND DISCUSSION

2.1. Synthesis of Mesoporous Microspheres. MTMs were prepared by combining sol−gel chemistry with polymer micro- and macrophase separation[33] as outlined in Figure 1. Although these processes occur simultaneously, they can be individually controlled by the choice of precursors, BCPs, and homopolymers. Therefore, our approach is both robust and tunable in terms of the meso- and macrostructures that can be produced. The pore network within the spheres originates from an interplay of BCP microphase separation and the sol−gel condensation reaction. In particular, the characteristic pore size lies in the nanometer range and is dictated by the molecular weight of the BCP. This concept can be used to fabricate mesostructured materials with a large range of pore sizes.[33,44] The spherical structure and its characteristic micrometer length scale arise from the macrophase separation of the homopolymer from the BCP−sol−gel composite. Its kinetic evolution depends on the molecular weight and compatibility of the components and on the details of the quenching protocol. Both processes are highly controllable, allowing the desired pore size (and thereby the specific surface area) and the average size of the spheres to be systematically dialed in.

We utilize an acid-stabilized sol−gel process that enables the TiO_2 precursors to selectively swell the hydrophilic block of a BCP[32] (see the Experimental Section for details). To demonstrate the versatility of our approach, two different BCP−homopolymer systems were employed (Table 1). Our process starts from a mixture containing the sol−gel precursors, a BCP, and a homopolymer (Figure 1a). Controlled evaporation of this solution produces self-assembled composite titania-BCP microspheres embedded in a homopolymer matrix (Figure 1b). The microphase separation of the BCP confines the titania precursor to a mesostructure. Simultaneously, the homopolymer phase separates from the titania-BCP composite through spinodal decomposition, affording a secondary structure on the micrometer scale. A similar concept has previously been applied to induce hierarchical morphologies by self-assembly processes.[16,33,45]

Table 1. Synthesis of the Different MTMs

sample	solvent	BCP	homopolymer	protocol
MTM-S	1:1 (v/v) toluene/IPA	PEO-*b*-PPO-*b*-PEO (5.8 kg/mol)	PMMA (15 kg/mol)	400 °C for 1 h, 2 °C/min
MTM-M	1:1 (v/v) THF/chloroform	PS-*b*-PEO (25.5 kg/mol)	PI (38 kg/mol)	500 °C for 2 h, 2 °C/min
MTM-L	1:1 (v/v) THF/chloroform	PS-*b*-PEO (74.5 kg/mol)	PI (38 kg/mol)	500 °C for 2 h, 2 °C/min
MTM-M/C	1:1 (v/v) THF/chloroform	PS-*b*-PEO (25.5 kg/mol)	PI (38 kg/mol)	600 °C for 2 h under argon, 2 °C/min, after homopolymer extraction
MTM-L/C	1:1 (v/v) THF/chloroform	PS-*b*-PEO (74.5 kg/mol)	PI (38 kg/mol)	600 °C for 2 h under argon, 2 °C/min, after homopolymer extraction

In contrast to these studies, we tune the macrophase separation in such a way that the microphase-separated structures are confined in micrometer-sized spheres. While low molecular weight additives may selectively swell one of the BCP blocks,[46] the high molecular weight homopolymer used in this study strongly phase separates from the BCP, for entropic reasons. The choice of homopolymers to induce phase separation is important because it allows us to control the phase separation process through their molecular weights and it significantly increases the variety of homopolymer-solvent couples that can be used. Therefore, a range of hierarchical morphologies can be realized, ranging from macroporous holes[45] (Swiss-cheese-like structures, Figure S1a, Supporting Information) via bicontinuous frameworks[16] (Figure S1b) to mesostructured microspheres confined in a polymeric matrix.

The formation of anatase can be achieved by direct calcination in air, which burns off the polymers and crystallizes the titania, forming MTMs (Figure 1c). Alternatively, the homopolymer can be dissolved prior to the heat treatment (Figure 1d). Subsequent pyrolysis under an inert atmosphere results in carbon-coated mesopores (Figure 1e) caused by the carbonization of the BCP, providing an electronically conductive scaffold that also stabilizes the mesostructure. Our approach can be applied to a range of precursors, BCPs, and homopolymers to change the composition and structural features of the material in a controlled fashion. In this paper, we focus on varying the mesopore size by employing different BCPs, in terms of chemical composition and molecular weight. The homopolymers were selected for their high solubility in the BCP−precursor−solvent mixture,[44] which is a key requirement to trigger phase separation into micrometer-sized spheres. Macrophase separation creates polydisperse morphologies with a size distribution around a characteristic feature size, as confirmed by dynamic light scattering measurements (Figure S2, Supporting Information). Note that polydisperse microspheres have higher packing densities compared to monodisperse spheres,[47] allowing higher volumetric energy densities to be achieved for battery electrodes.

We studied MTMs with three different pore sizes, two of which were in situ carbon-coated. Table 1 summarizes the different solvents, BCPs, and homopolymers used for the syntheses of the different MTMs and their heat treatment protocols. The low molecular weight poly(ethylene oxide-*block*-propylene oxide-*block*-ethylene oxide) (PEO-*b*-PPO-*b*-PEO, Pluronic) BCP with its weak segregation between its polymeric blocks results in microspheres with relatively small mesopores (MTM-S), as demonstrated by scanning electron microscopy (SEM) images (Figure 2a,b). The higher molecular weight poly(styrene-*block*-ethylene oxide) (PS-*b*-PEO) BCPs with higher incompatibility between their blocks form medium-sized (MTM-M, Figure 2c, and MTM-M/C, Figure S6a,b, Supporting Information) and large (MTM-L, Figure 2d, and MTM-L/C, Figure S6c,d) pores, with increasing molecular weight.

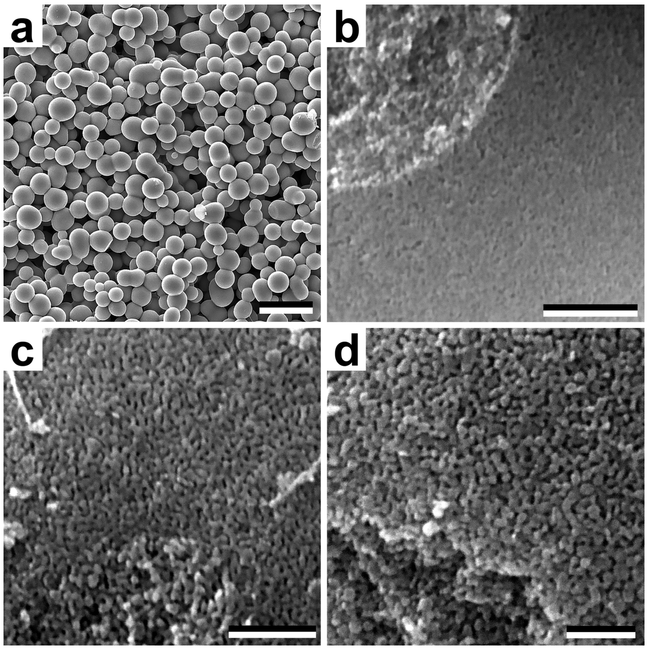

Figure 2. SEM images of MTMs with different pore sizes. (a) Low-magnification image showing the spherical shape of MTM-S particles. The scale bar represents 5 μm (similar images for the other MTMs are shown in Figure S3, Supporting Information). (b−d) High-magnification images showing the mesostructure of (b) MTM-S, (c) MTM-M, and (d) MTM-L. The scale bars represent 200 nm.

2.2. Morphological Characterization.

To quantify the morphological differences between different MTMs, we performed SEM, small-angle X-ray scattering (SAXS), and physisorption measurements. The results are summarized in Table 2. The spherical shape of the particles is evident from the SEM images, and their mesoporosities are clearly discernible (Figure 2 and Figures S3 and S5, Supporting Information). MTMs that were annealed in an argon atmosphere, leading to a carbon-coated pore structure, are similar in appearance to their uncoated counterparts (Figure S6, Supporting Information). The SAXS profiles (Figure 3) show a single peak for each sample.

Table 2. Morphological Characteristics of Different MTMs

sample	characteristic period of the structure (SAXS) (nm)	specific surface area (BET) (m^2/g)	average pore size (BJH) (nm)	average crystallite size (XRD) (nm)
MTM-S	13.6	201	3.05	4.2
MTM-M	17.8	65.3	6.98	8.2
MTM-L	40.3	37.7	11.8	9.6
MTM-M/C	18.6	63.6	6.76	6.0
MTM-L/C	33.8	37.7	12.6	6.5

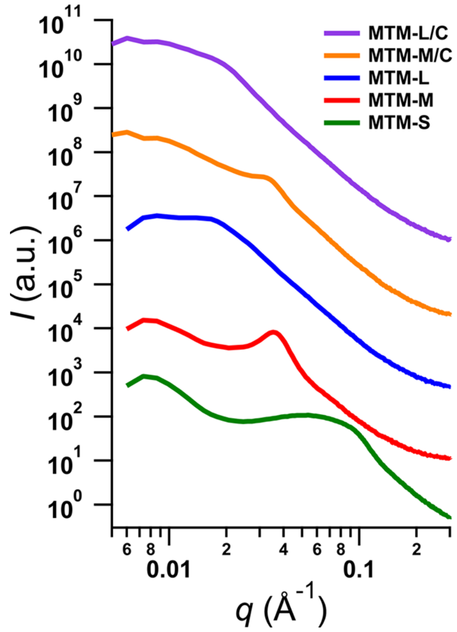

Figure 3. SAXS profiles of different MTMs.

Its position determines the characteristic dimension of the respective mesostructure, ranging from 13.6 nm (MTM-S) to 40.3 nm (MTM-L). The absence of sharper and higher order peaks indicates a lack of long-range order and is typically observed for short-range-ordered wormlike mesostructures (cf. Figure 2).[37] The comparatively broad shoulder in the MTM-S SAXS data may arise from a lower structural stability of the material during calcination, leading to a lower degree of order. Physisorption measurements (Figure 4) show that the specific surface area calculated by the Brunauer−Emmett−Teller (BET) analysis[48] increases with decreasing structure size. Furthermore, the average pore size determined by the Barrett−Joyner−Halenda (BJH) method[49] increases from 3.05 nm (MTM-S) to 11.8 nm (MTM-L) when higher molecular weight BCPs are employed, demonstrating the large range of pore sizes accessible by our approach. A focused ion beam (FIB) was used to cut a thin slice from an MTM-M microsphere, which allowed the imaging of its interior morphology by transmission electron microscopy (TEM) (Figure S4, Supporting Information). A homogeneous mesostructure can be observed throughout the microspheres, demonstrating that the spheres are porous both internally and externally (cf. Figure 2).

When the sol−gel-derived material is heated, the average grain size of the TiO_2 crystallites in the mesostructured composites is controlled by the temperature.[50] This in principle allows the adjustment of the crystallite size irrespective of the pore dimensions. The minimum temperatures for calcination are given by the necessity to degrade (or carbonize) all polymeric components to transform the composite into a mesoporous material. Thermogravimetric analysis (TGA) data (Figure S7, Supporting Information) show that temperatures above 400 °C are needed for the formation of MTM-S and temperatures above 450 °C are required for MTM-M and MTM-L. It is known that crystal growth during annealing can lead to a collapse of the mesopore morphology,[34,38,50] particularly in materials with small pores. To prevent this, the relatively low calcination temperature of 400 °C and a calcination time of 1 h were used for the MTM-S sample. The resulting crystallite size, evaluated by applying the Scherrer equation[51] to the X-ray diffraction (XRD) data (Figure 5), was 4.2 nm. Higher temperatures or longer annealing times led to a reduction of the specific surface area (Figure S8, Supporting Information), indicating a loss of porosity.

The medium and large mesopores are, on the other hand, more stable during heat treatment. An annealing temperature of 500 °C for 2 h formed larger crystallite sizes (Table 2) while maintaining the mesostructure. Higher calcination temperatures and longer annealing times generally result in a higher degree of crystallinity[8,12,44] and better electronic conductivities of the materials.[50]

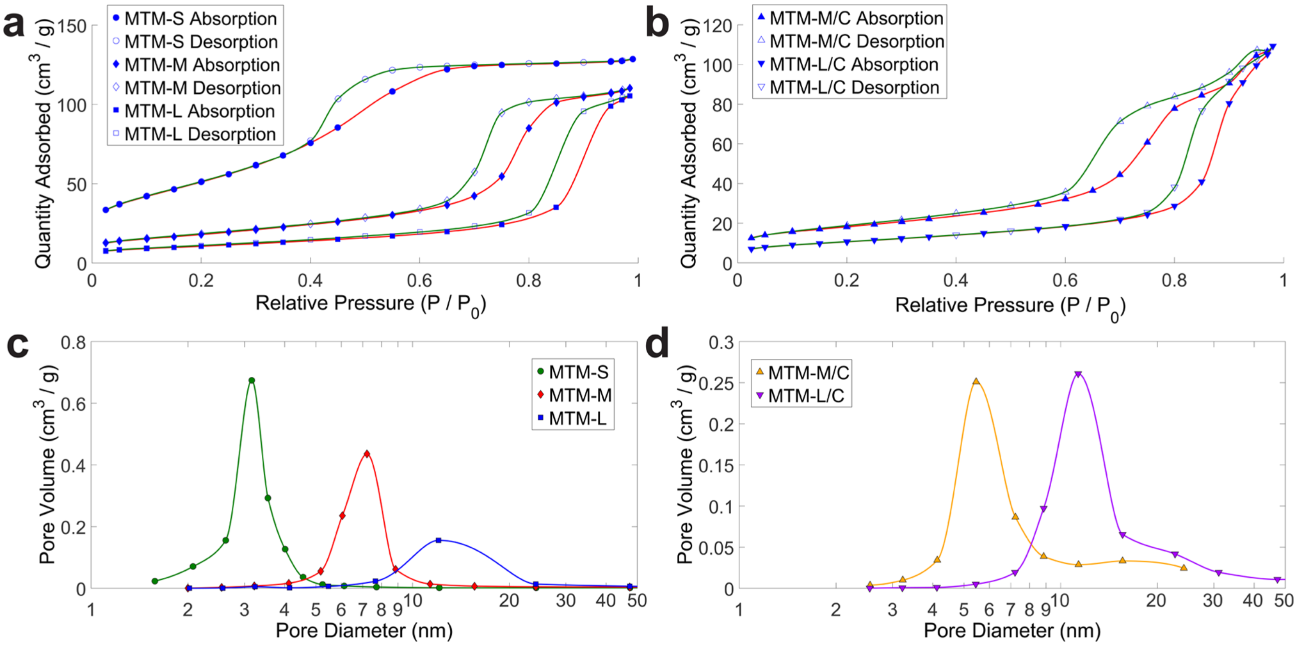

Figure 4. (a, b) Physisorption isotherms for MTMs (a) without and (b) with a carbon coating. (c, d) Corresponding pore-size distributions determined by applying the BJH method to the desorption branch of the respective isotherms.

DOI: 10.1021/acsami.7b03155
ACS Appl. Mater. Interfaces 2017, 9, 22388−22397

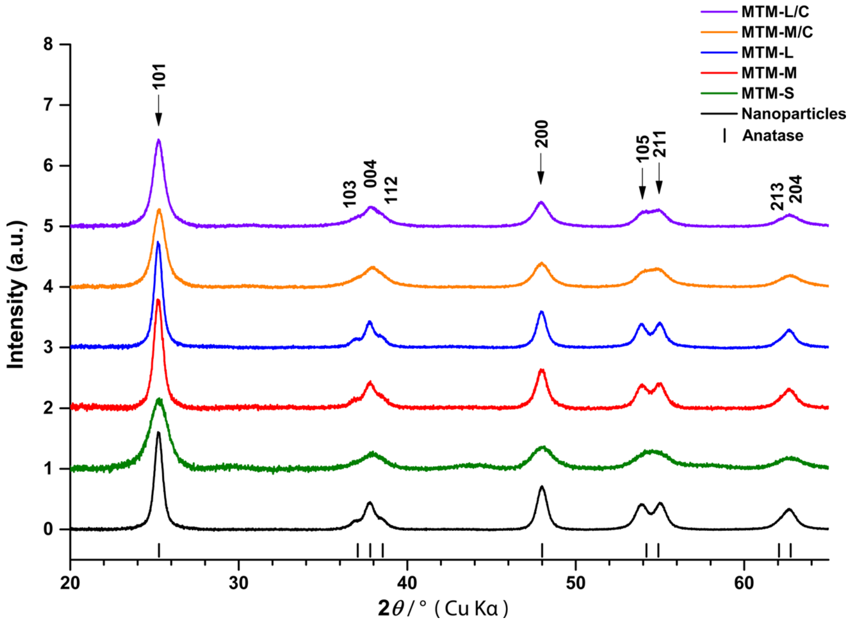

Figure 5. XRD patterns of different MTMs and commercial titania nanoparticles. Main reflections from the anatase phase are labeled using vertical bars for comparison. The peaks are all indexed with the ones that are used for crystallite size evaluation marked with arrows.

To stabilize mesoporous materials during annealing at high temperatures, a sacrificial silica source has been added to the precursor solution in some studies.[16,38] Alternatively, a carbon coating on the mesopores can be employed to mechanically support the pore morphology at high temperatures while simultaneously facilitating electron transport.[26,37,43] Carbon coatings can be fabricated in situ for BCPs containing sp^2-bonded polymeric blocks, which carbonize to form a thin carbon layer on the surface of the metal oxide[43] (Figure 1e). This is the case for the PS block of the PS-*b*-PEO copolymer.

To prevent the additional carbon formation between the spheres, the PI homopolymer was dissolved in cyclohexane prior to the heat treatment. Pyrolysis of the TiO_2-BCP microspheres under an inert atmosphere resulted in microspheres with carbon-coated mesopores. A temperature of 600 °C was chosen because higher temperatures may induce a phase transition from anatase to rutile,[52] which is typically accompanied by a loss of the mesostructure.[50] On the one hand, the phase transition temperature typically varies inversely with the crystallite size.[53] A carbon coating on the MTMs presents a spatial confinement of the material which generally results in smaller crystallite sizes[43] (cf. Table 2). On the other hand, the phase transition temperature is lowered in the presence of oxygen defects that form during annealing in an inert atmosphere, in particular in the presence of carbon.[54] The combination of these effects resulted in a phase transition temperature between 600 °C (pure anatase) and 650 °C (significant formation of rutile impurities) for our carbon-coated samples. Raman spectra confirm the formation of the anatase phase and the presence of carbon in the pyrolyzed samples (Figure S9, Supporting Information). TGA data of carbon-coated MTMs suggest a carbon weight fraction of 9 wt % (MTM-L/C) and 10 wt % (MTM-M/C) in the respective mesopore structures (Figure S10, Supporting Information). High-resolution TEM reveals the presence of a 1.0−1.5 nm thick carbon coating covering the mesopores (Figure S11, Supporting Information).

2.3. Electrochemical Performance. In contrast to carbonaceous electrodes, the insertion of lithium into anatase takes places above 1 V vs Li/Li^+. On one hand, a higher voltage anode leads to a lower cell voltage and therefore a reduced energy density when applied in a full cell. On the other hand, it improves the safety of the battery by reducing the risk of lithium plating. In addition, the higher operating voltage of anatase minimizes electrolyte decomposition and the associated formation of a solid−electrolyte interface (SEI). Mitigating these surface-related reactions is particularly beneficial for nanostructured materials due to their large surface areas.[12,14,15,37]

Figure 6 shows the electrochemical performance of MTMs with different pore sizes under galvanostatic conditions. Compared to commercial titania nanoparticles (with a specific surface area between those of MTM-M and MTM-L; see the Experimental Section), all MTMs demonstrate improved rate performance and capacity retention. This can be ascribed to the hierarchical structure that provides efficient pathways for electronic and ionic conduction.[15] In addition, MTMs are less likely to detach from the conductive support upon volume changes that occur during (de)lithiation of the active materials, which is the main cause for the capacity losses during cycling in electrodes comprising nanoparticles. MTMs seem to suffer much less from this effect. Long-term cycling data (Figure S12, Supporting Information) support this observation. Nanoparticle electrodes show significant capacity losses, whereas MTMs generally demonstrate better capacity retention. Nevertheless, MTMs of different pore sizes differ significantly in terms of their cyclabilities. MTM-S displays a very pronounced capacity drop over 250 cycles at a rate of 1C. MTM-M is much more stable during cycling but still demonstrates a gradual decrease in capacity. MTM-L shows the best capacity retention. These observations indicate that the smaller specific surface areas of MTMs with larger pore sizes improve the cycling stability of the material.

A rate performance comparison of the MTMs (Figure 6a) shows that MTMs with smaller pore sizes have higher capacities during the first few cycles. While the capacity retention of MTM-M and MTM-L follows a similar steady reduction when the rate increases, the drop in capacity is much more pronounced

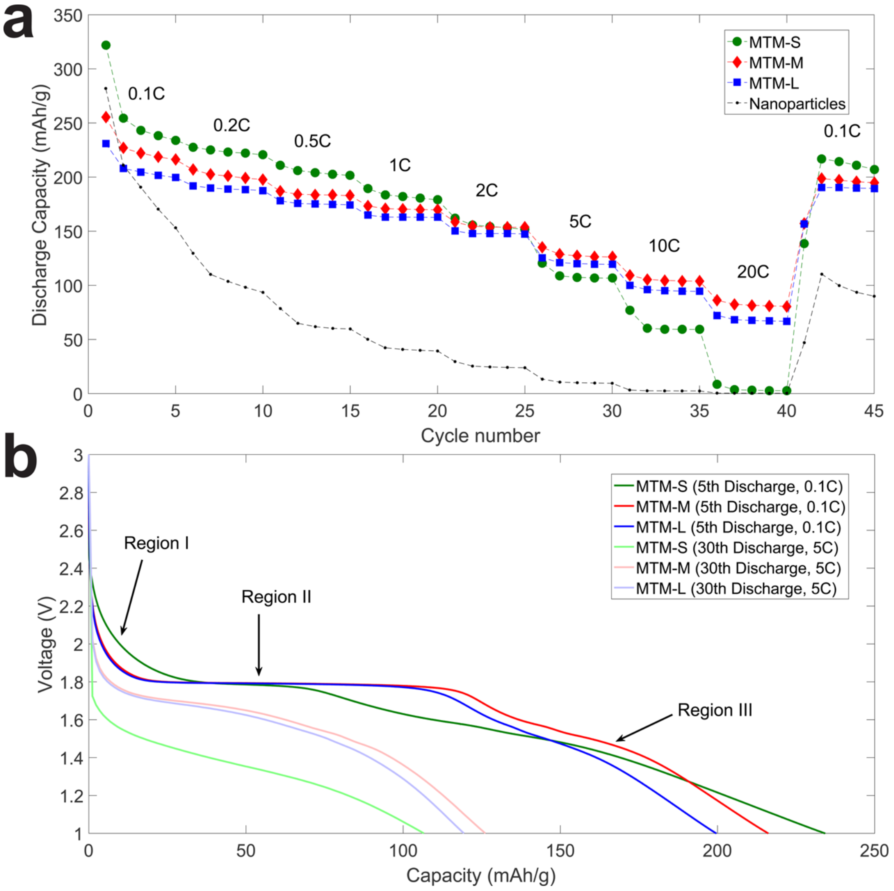

Figure 6. Electrochemical performance of titania nanoparticles and MTMs with different pore sizes, obtained from galvanostatic cycling at different rates. (a) Discharge capacities at various rates. (b) Galvanostatic discharge curves of selected cycles and rates.

for MTM-S, particularly at rates of 10C and higher. These results are in agreement with other reports on porous anatase spheres.[8,9,12] In more detail, MTM-S exhibits a similarly pronounced capacity drop at higher rates compared to other mesoporous TiO_2 microspheres that were prepared using relatively low annealing temperatures.[8] In the case of anatase microspheres treated at higher temperatures, the advantage of large surface areas for both the low rate capacity and its retention at higher rates was previously studied[9] and is in agreement with our results for MTM-M and MTM-L. However, our MTMs have higher capacities than what would be expected from a comparison of their specific surface areas alone. When compared to monodisperse microspheres[12] with morphological properties that come closest to those of our MTMs (15 nm pore width, 2.1 μm diameter), we observe comparable capacities, both at a rate of 0.1C and at 20C. The carbon-coated MTMs display cyclabilities (Figure S12, Supporting Information) and rate behaviors (Figure S13a, Supporting Information) similar to those of their uncoated analogues but have higher capacities. This is particularly evident at lower rates and is possibly caused by their smaller crystallite sizes[55] (cf. Table 2).

The increasing initial capacity with decreasing pore size can be ascribed to the larger surface-to-volume ratio of the samples (Table 2). An increase in surface area has been shown to increase the capacity of titania anodes due to capacitative contributions[17,56,57] and (partly irreversible) interfacial processes.[26,58,59] A higher insertion capacity for smaller particle sizes has also been demonstrated and was explained by the enhanced solid-solution behavior in nanosized anatase particles.[53,55] Generally, an increased lithium uptake is ascribed to regions within a few nanometers from the particle surface,[14] revealing the advantage of larger surface-to-volume ratios. This arises from a low diffusion coefficient for lithium ions in the lithiated anatase structure preventing further lithium insertion beyond the particle surface.[31,60] The larger surface areas of smaller pores also add to the comparatively large capacity drop from the first to the second cycle (MTM-S) due to irreversible reactions involving surface-adsorbed species.[14,58,61] These irreversible contributions can also be observed in cycle life tests (Figure S12, Supporting Information). The first discharge cycles display significantly higher capacities than the following cycles. On one hand, the undesirable capacity losses from the first to the second cycle are more pronounced for larger surface areas. On the other hand, larger surface areas result in larger reversible capacities (cf. the first few cycles in Figure 6a and in Figure S12). We note that all samples studied in this paper possess mesoporous structures with large surface areas and therefore demonstrate significantly higher capacities than nonporous (micro)particles (cf. Figure S14, Supporting Information).

Recent studies on anatase nanomaterials have suggested that a division of the galvanostatic discharge curves into three distinct regions can be used to estimate the contribution from the electrode surface area to the charge storage.[12,26,59] Figure 6b and Figure S13b (Supporting Information) demonstrate this concept for different MTMs. The discharge curves of the fifth cycle (0.1C) are depicted since they are less influenced by irreversible reactions compared to the first few cycles. Furthermore, the different kinetic performances of the MTMs have a much smaller effect on the discharge behavior of this low-rate cycle in comparison to cycles that have been conducted at a higher rate (cf. the depicted 30th cycle at 5C). The first region describes the initial voltage drop between 3 and ~1.8 V (region I), which is associated with the formation of a conductive Li_xTiO_2 phase in a solid−solution process.

The following voltage plateau (region II) corresponds to a two-phase insertion reaction from the tetragonal anatase to the orthorhombic $Li_{0.5}TiO_2$ phase. The extent of region II is apparently related to the degree of crystallinity of the MTMs (cf. Table 2). The similar crystallite sizes of MTM-M and MTM-L (due to the same heat treatment) give rise to nearly equivalent two-phase plateaus. A similar observation can be made between the carbon-coated analogues of these MTMs. Relative to their non-carbon-coated counterparts, they show a slightly reduced two-phase region, in agreement with their smaller crystallite sizes. MTM-S had to be calcined at a lower temperature than the other MTMs to preserve its mesostructure and is therefore distinctly less crystalline than the other samples. Therefore, MTM-S displays a much smaller two-phase plateau, in accordance with its small crystallite size. The reduction in capacity in region II typically contributes to larger capacities in the other regions, as observed for studies on amorphous TiO_2.[58] We note that structural changes that occurred during prolonged annealing of MTM-S led to a considerable reduction of the electrochemical performance (Figure S14, Supporting Information), indicating that the pores were no longer completely accessible to the electrolyte.

The subsequent slope in the galvanostatic curve is labeled as region III. Lithium storage in this region has been shown to be surface-dependent.[12,14,26,31,59] It is evident that the extent of region III increases for smaller pores sizes, confirming that the additional capacity is linked to the their larger surface-to-volume ratio. A complete set of charge and discharge curves for all MTMs at various rates can be found in Figures S15 and S16 (Supporting Information). Figures S17 and S18 (Supporting Information) quantify the contributions of the different regions in these curves to their overall capacity, confirming the general validity of our discussion. A closer examination of region III reveals the presence of two subtle plateaus which are particularly pronounced in the case of MTM-S (differential capacity curves are shown in Figure S19, Supporting Information). These features are located between 1.4 and 1.6 V vs Li/Li^+ and can possibly be assigned to the TiO_2(B) phase,[62] a common minor component in TiO_2 materials synthesized by sol−gel chemistry.[61] The XRD pattern of MTM-S also hints toward the presence of this phase (Figure S20, Supporting Information).

To understand the kinetic effects responsible for the differences in capacity retention at high rates between various MTMs, it is instrumental to examine the rate dependence of their overpotentials. Figure 6b shows the voltage drop of MTMs when the current rate increases from 0.1C to 5C. MTM-S exhibits a larger drop compared to MTM-M and MTM-L. This behavior can be quantified by investigating how the plateau voltage associated with the two-phase reaction (region II) changes with increasing cycling rate (Figure S21, Supporting Information). Charge transfer and ohmic polarizations contribute to the overpotential, but no concentration polarization is observed, indicating that ion transport in the electrolyte is not a limiting factor in our experiments. Therefore, larger pore sizes have no apparent benefit for the kinetics of the electrode. Furthermore, it can be seen that MTM-M shows slightly less polarization than MTM-L, which can be explained by lower charge-transfer resistances due to an increased surface area.[12,14,59] This also holds true for the carbon-coated samples. Although the even larger specific surface area of MTM-S should in principle further improve the charge-transfer kinetics of the electrode, the sample instead shows a much larger (ohmic) polarization. We attribute this to the lower electric conductivity of the active material, stemming from its poorer crystallinity compared to those of the other MTMs.[12,50]

The carbon-coated MTMs show slightly larger polarization than their uncoated counterparts, indicating that the conductive coating is not able to reduce the ohmic overpotential despite the superior electrical conductivity of (graphitic) carbon compared to pristine TiO_2. Due to the relatively uniform (cf. Figure S11, Supporting Information) and partly graphitic (cf. Figure S9, Supporting Information) nature of the carbon coating, an improved electrochemical performance of the respective MTMs is expected. The fact that the carbon coating has no considerable effect on the MTM performance can be explained by the lithium insertion into anatase, which substantially increases its conductivity.[63,64] This reduces the need for an additional highly conducting material. Note that annealing in an inert atmosphere resulted in the formation of smaller crystallites for the carbon-coated MTMs compared to their respective counterparts that have been calcined in air (Table 2). The smaller crystallite size may be detrimental for the conductivity of the material, explaining the higher overpotentials. Additionally, the in situ formed carbon provides a reducing environment, which was shown to alter the electrochemical properties of anatase.[65] Electrochemical impedance spectroscopy (EIS) corroborates our findings (Figure S22, Supporting Information). MTM-M and MTM-M/C show smaller charge-transfer resistances than MTM-L and MTM-L/C due to their higher specific surface areas. MTM-S however suffers from a much higher impedance, as a result of its poor electronic conductivity. Carbon-coated MTMs show a slightly different impedance behavior compared to the uncoated MTMs with reduced charge-transfer resistances, possibly resulting from the carbon coating or their smaller crystallite sizes.

3. CONCLUSION

In summary, we present a novel and facile method to synthesize MTMs. Combining BCP-directed sol−gel chemistry with polymer phase separation produces mesostructured spherical particles in the micrometer range. The approach is applicable to BCPs with various molecular weights and different chemical compositions, thus allowing the mesopore sizes to be tuned over a wide range. It also allows the surface of the pores to be coated with conductive carbon in situ. When employed as anode materials in LIBs, the MTMs show significantly improved performances compared to electrodes made from titania nanoparticles. We further studied the impact of different pore sizes and carbon coatings on the electrochemical behavior. Smaller pores imply larger surface-to-volume ratios, i.e., lower charge-transfer resistances and reduced diffusion pathways, thereby improving the kinetics of the electrode. However, larger surface areas augment side reactions resulting in increased irreversible capacity losses during the first cycle and a more pronounced capacity fading during long-term cycling. Most importantly, the manufacture of spheres with the smallest pores requires a heat treatment at relatively low temperatures, since anatase crystallization at higher temperatures destroys the pore structure. This results in a lower crystallinity, and the associated reduced conductivity significantly decreases the high-rate performance. Therefore, spheres with medium pore sizes (MTM-M) displayed the best capacity retention at high rates among the studied samples. The high conductivity of lithiated anatase renders an in situ formed carbon coating superfluous. Importantly, the presented approach combining BCP self-assembly, sol−gel chemistry, and polymer macrophase separation is generic and in principle transferable to other inorganic compounds. In this respect, the in situ carbon formation may be beneficial for the synthesis of hierarchical electrode materials with very low intrinsic conductivities, such as lithium iron phosphate or lithium titanate.

4. EXPERIMENTAL SECTION

4.1. General Synthesis Concept for MTMs. The sol−gel solutions were created by mixing concentrated hydrochloric acid (37 wt % HCl in H_2O) and titanium tetraisopropoxide (TTIP) in a solvent with a molar ratio of TTIP:HCl:H_2O = 1:1.19:4.0. A BCP solution and a homopolymer solution were added to the sol−gel solution such that the final weight ratio of TiO_2:BCP:homopolymer was 2:1:5. The solutions were left to stir for several hours before being evaporated in a Petri dish (9 cm diameter) on a hot plate set to 50 °C (cf. Figure S23, Supporting Information). The samples were further aged for several days before annealing. Poly(styrene-*block*-ethylene oxide) block copolymers were purchased from Polymer Source Inc. All other chemicals were purchased from Sigma-Aldrich and used as received.

4.1.1. Synthesis of Small-Pore Microspheres (MTM-S). Concentrated hydrochloric acid (0.241 mL) was added to a 1:1 (v/v) mixture of toluene and isopropyl alcohol (IPA) (7.018 mL). TTIP (0.741 mL) was then added to this solution under vigorous stirring. A solution of poly(ethylene oxide)-*block*-poly(propylene oxide)-*block*-poly(ethylene oxide) (PEO-*b*-PPO-*b*-PEO, Pluronic P-123; 5.8 kg/mol, 30 wt % PEO) in 1:1 (v/v) toluene/IPA (50 g/L, 2 mL) and a poly(methyl methacrylate) (PMMA; 15 kg/mol) solution in 1:1 (v/v) toluene/IPA (50 g/L, 10 mL) were added to the sol−gel solution. After evaporation (20 mL per Petri dish), the product was calcined at 400 °C for 1 h (2 °C/min ramp) in air.

4.1.2. Synthesis of Medium-Pore (MTM-M) and Large-Pore (MTM-L) Microspheres. Concentrated hydrochloric acid (0.241 mL) was added to THF (7.018 mL). TTIP (0.741 mL) was subsequently added to this solution under vigorous stirring. A poly(styrene-*block*-ethylene oxide) (PS-*b*-PEO; MTM-M, 25.5 kg/mol, 25 wt % PEO; MTM-L, 74.5 kg/mol, 19 wt % PEO) stock solution (50 g/L in THF, 2 mL) and a poly(isoprene) (PI; 38 kg/mol, *cis*, made from natural rubber) solution (50 g/L in chloroform, 10 mL) were slowly added. After evaporation (10 mL per Petri dish), calcination was performed at 500 °C for 2 h (2 °C/min ramp) in air.

4.1.3. Synthesis of Carbon-Coated Medium-Pore (MTM-M/C) and Large-Pore (MTM-L/C) Microspheres. The synthesis of MTM-M/C and MTM-L/C followed the aforementioned procedure for MTM-M and MTM-L, respectively, up to the calcination step. In this case, the PI homopolymer in the composite was dissolved in cyclohexane and extracted through multiple filtration and redissolution steps. To prevent structural damage (cf. Figure S24, Supporting Information), residual cyclohexane was removed by a freeze-drying step. The composite was then annealed under flowing argon in a tube furnace at 600 °C for 2 h (2 °C/min ramp).

4.2. Characterization Techniques. The micro- and mesostructures of MTMs were imaged with a Tescan Mira 3 LMH scanning electron microscope. X-ray diffraction (XRD) was performed using a Rigaku Ultima IV with a copper target. LaB_6 was used as an external reference to obtain the instrumental broadening. Physisorption measurements for the calculation of specific surface areas (BET) and pore size distributions (BJH) were conducted with a Micromeritics Gemini V surface area analyzer using nitrogen as the adsorbate. To determine the characteristic period of the mesostructure, we employed small-angle X-ray scattering (SAXS) using a Rigaku NanoMAX-IQSAXS camera equipped with a Cu target sealed tube source (MicroMax 003 microfocus from Rigaku). The scattering data were collected using a Pilatus100 K detector (Dectris). The sample-to-detector distance was calibrated using a silver behenate standard. Thermogravimetric analysis (TGA) was performed with a Mettler Toledo system using an Al crucible and a temperature range of 60−600 °C with a heating rate of 5 °C/min. Dynamic light scattering (DLS) measurements were performed with a 3D LS spectrometer (LS Instruments AG) equipped with a linearly polarized and collimated laser beam operating at 660 nm (Cobolt 05-01 diode-pumped solid-state laser, $P_{\max}$ = 500 mW) to determine the distribution of the microsphere radii. The measurements were performed at scattering angles of 90° and 150° for 60 s at a temperature of 25 °C. Raman measurements were conducted using a Horiba LabRAM HR800 system and a laser wavelength of 532 nm. All signals were baseline corrected, smoothed, and normalized at 637.2 cm^{-1}. Samples processed via a focused ion beam (FIB) were electrostatically adhered to copper FIB lift-out grids and were prepared in an FEI Quanta 200 3D FIB scanning electron microscope. Platinum was deposited from the gas phase in the form of trimethyl(methylcyclopentadienyl)platinum(IV), delivered from an internal gas injector with a crucible temperature of 44 °C at a working distance of approximately 1 mm. Ion milling was performed at 30 kV, with currents between 1 nA and 30 pA. Transmission electron microscopy (TEM) and high-resolution TEM images were obtained at room temperature using JEOL 2100Plus LaB_6 and JEOL 2100F transmission electron microscopes, respectively, operating at an accelerating voltage of 200 kV. Images were acquired using Gatan US1000 and Gatan Orius charge-coupled device (CCD) cameras, respectively.

4.3. Electrochemical Characterization. To fabricate electrode films for LIBs, the MTMs were mixed with conductive carbon black (Timcal Super C65) and a poly(vinylidene fluoride) (PVdF, Kynar) binder in a weight ratio of 80:10:10. 1-Methyl-2-pyrrolidinone (NMP; 2.5 μL/g of mixture) was added to produce a homogeneous paste that was cast on Al foils. The loading of the active material was 0.67 ± 0.09 mg/cm^2. Circular electrodes were cut and dried at 80 °C under vacuum overnight and transferred to an argon-filled glovebox (MBraun Labmaster Pro) where they were assembled in Swagelok cells with lithium metal (thickness 0.75 mm) as the counter electrode. $LiPF_6$ (1.0 M) in 1:1 (v/v) ethylene carbonate (EC)/ethyl methyl carbonate (EMC) (battery grade) was used as the electrolyte, and a glass fiber disk (Whatman, grade GF/B) was used as a separator. Anatase nanopowder (<25 nm particle size, specific surface area 45−55 m^2/g) was used as a reference electrode material. Galvanostatic cycling was performed at room temperature using an Arbin BT 2043 to examine the rate performance of the cells. Electrochemical impedance spectroscopy (EIS) was performed using a Metrohm Autolab PGSTAT302N. After the galvanostatic rate performance tests were completed, the cells were discharged to 1 V vs Li/Li^+ at a rate of ~1C and EIS measurements were conducted with an amplitude of 10 mV. A frequency range from 1 MHz to 1 Hz was employed with 20 data points taken per decade.

■ ASSOCIATED CONTENT

Ⓢ Supporting Information

The Supporting Information is available free of charge on the ACS Publications website at DOI: 10.1021/acsami.7b03155.

> SEM images of other macrophase-separated morphologies, (carbon-coated) MTMs, and collapsed microspheres, DLS data, TEM image of the internal MTM structure, HR-TEM image of the carbon coating, TGA data of polymers and carbon-coated MTMs, calcination time-dependent specific surface area of MTM-S, Raman data, electrochemical cycle life study, electrochemical rate performance of carbon-coated MTMs and structurally collapsed MTM-S, galvanostatic (dis)charge curves at various rates, analysis of the contributions of different electrochemical processes to the overall capacity, differential capacity plot, detailed XRD analysis of MTM-S, overpotential analysis, EIS data (Nyquist plot), and schematic of the evaporation conditions (PDF)

AUTHOR INFORMATION

Corresponding Authors

*E-mail: xiao.hua@unifr.ch.

*E-mail: ullrich.steiner@unifr.ch.

ORCID

Michael G. Fischer: 0000-0002-0519-5463

Bodo D. Wilts: 0000-0002-2727-7128

Ilja Gunkel: 0000-0001-5738-5309

Ullrich Steiner: 0000-0001-5936-339X

Notes

The authors declare no competing financial interest.

ACKNOWLEDGMENTS

We thank Samuel Roth (HEIA Fribourg) for performing the Raman measurements used in this paper. We gratefully acknowledge the University of Nottingham Nanoscale and Microscale Research Centre (NMRC) for access to their instrumentation, in particular Dr. Christopher D. J. Parmenter for assistance with FIB-SEM sample preparation and Dr. Michael W. Fay for assistance with TEM imaging on the JEOL 2100 instruments. We also thank Preston H. Sutton and Jonathan H. W. Lim for discussions. Funding from the Swiss National Science Foundation through the NRP70 program (Grant 153764) and Ambizione (Grant 168223 to B.D.W.) and from the Adolphe Merkle Foundation is gratefully acknowledged. This project has also received funding from the European Union's Horizon 2020 research and innovation program under Marie Skłodowska-Curie Grant Agreement No. 706329/cOMPoSe (to I. G.). We also acknowledge funding from the University of Nottingham Engineering and Physical Sciences Partnered Access Fund for supporting our use of the NMRC facilities.

REFERENCES

(1) Pan, J. H.; Cai, Z.; Yu, Y.; Zhao, X. S. Controllable Synthesis of Mesoporous F-TiO_2 Spheres for Effective Pphotocatalysis. *J. Mater. Chem.* **2011**, *21*, 11430−11438.

(2) Li, B.; Shao, X.; Hao, Y.; Zhao, Y. Ultrasonic-Spray-Assisted Synthesis of Metal Oxide Hollow/Mesoporous Microspheres for Catalytic CO Oxidation. *RSC Adv.* **2015**, *5*, 85640−85645.

(3) Chen, D.; Huang, F.; Cheng, Y.-B.; Caruso, R. A. Mesoporous Anatase TiO_2 Beads with High Surface Areas and Controllable Pore Sizes: A Superior Candidate for High-Performance Dye-Sensitized Solar Cells. *Adv. Mater.* **2009**, *21*, 2206−2210.

(4) Chen, W.; Qiu, Y.; Yan, K.; Yang, S. Surfactant Directed Self-Assembly of Size-Tunable Mesoporous Titanium Dioxide Microspheres and their Application in Quasi-Solid State Dye-Sensitized Solar Cells. *J. Power Sources* **2011**, *196*, 10806−10816.

(5) Guo, E.; Yin, L. Nitrogen Doped TiO_2-Cu_xO Core-Shell Mesoporous Spherical Hybrids for High-Performance Dye-Sensitized Solar Cells. *Phys. Chem. Chem. Phys.* **2015**, *17*, 563−574.

(6) Liu, Y.; et al. Radially Oriented Mesoporous TiO_2 Microspheres with Single-Crystal−like Anatase Walls for High-Efficiency Optoelectronic Devices. *Sci. Adv.* **2015**, *1*, e1500166.

(7) Das, S. K.; Darmakolla, S.; Bhattacharyya, A. J. High Lithium Storage in Micrometre Sized Mesoporous Spherical Self-Assembly of Anatase Titania Nanospheres and Carbon. *J. Mater. Chem.* **2010**, *20*, 1600−1606.

(8) Wang, J.; Zhou, Y.; Hu, Y.; O'Hayre, R.; Shao, Z. Facile Synthesis of Nanocrystalline TiO_2 Mesoporous Microspheres for Lithium-Ion Batteries. *J. Phys. Chem. C* **2011**, *115*, 2529−2536.

(9) Ma, Y.; Ji, G.; Ding, B.; Lee, J. Y. Facile Solvothermal Synthesis of Anatase TiO_2 Microspheres with Adjustable Mesoporosity for the Reversible Storage of Lithium Ions. *J. Mater. Chem.* **2012**, *22*, 24380−24385.

(10) Shen, J.; Wang, H.; Zhou, Y.; Ye, N.; Li, G.; Wang, L. Anatase/Rutile TiO_2 Nanocomposite Microspheres with Hierarchically Porous Structures for High-Performance Lithium-Ion Batteries. *RSC Adv.* **2012**, *2*, 9173−9178.

(11) Oh, S.-M.; Hwang, J.-Y.; Yoon, C. S.; Lu, J.; Amine, K.; Belharouak, I.; Sun, Y.-K. High Electrochemical Performances of Microsphere C-TiO_2 Anode for Sodium-Ion Battery. *ACS Appl. Mater. Interfaces* **2014**, *6*, 11295−11301.

(12) Rodriguez, E. F.; Chen, D.; Hollenkamp, A. F.; Cao, L.; Caruso, R. A. Monodisperse Mesoporous Anatase Beads as High Performance and Safer Anodes for Lithium Ion Batteries. *Nanoscale* **2015**, *7*, 17947−17956.

(13) Tahir, M. N.; Oschmann, B.; Buchholz, D.; Dou, X.; Lieberwirth, I.; Panthöfer, M.; Tremel, W.; Zentel, R.; Passerini, S. Extraordinary Performance of Carbon-Coated Anatase TiO_2 as Sodium-Ion Anode. *Adv. Energy Mater.* **2016**, *6*, 1501489.

(14) Wagemaker, M.; Mulder, F. M. Properties and Promises of Nanosized Insertion Materials for Li-Ion Batteries. *Acc. Chem. Res.* **2013**, *46*, 1206−1215.

(15) Bruce, P. G.; Scrosati, B.; Tarascon, J.-M. Nanomaterials for Rechargeable Lithium Batteries. *Angew. Chem., Int. Ed.* **2008**, *47*, 2930−2946.

(16) Hwang, J.; Jo, C.; Hur, K.; Lim, J.; Kim, S.; Lee, J. Direct Access to Hierarchically Porous Inorganic Oxide Materials with Three-Dimensionally Interconnected Networks. *J. Am. Chem. Soc.* **2014**, *136*, 16066−16072.

(17) Sudant, G.; Baudrin, E.; Larcher, D.; Tarascon, J.-M. Electrochemical Lithium Reactivity with Nanotextured Anatase-Type TiO_2. *J. Mater. Chem.* **2005**, *15*, 1263−1269.

(18) Tartaj, P.; Amarilla, J. M. Multifunctional Response of Anatase Nanostructures Based on 25 nm Mesocrystal-Like Porous Assemblies. *Adv. Mater.* **2011**, *23*, 4904−4907.

(19) Amarilla, J. M.; Morales, E.; Sanz, J.; Sobrados, I.; Tartaj, P. Electrochemical Response in Aprotic Ionic Liquid Eelectrolytes of TiO_2 Anatase Anodes Based on Mesoporous Mesocrystals with Uniform Colloidal Size. *J. Power Sources* **2015**, *273*, 368−374.

(20) Yang, X.; Yang, Y.; Hou, H.; Zhang, Y.; Fang, L.; Chen, J.; Ji, X. Size-Tunable Single-Crystalline Anatase TiO_2 Cubes as Anode Materials for Lithium Ion Batteries. *J. Phys. Chem. C* **2015**, *119*, 3923−3930.

(21) Chen, D.; Cao, L.; Huang, F.; Imperia, P.; Cheng, Y.-B.; Caruso, R. A. Synthesis of Monodisperse Mesoporous Titania Beads with Controllable Diameter, High Surface Areas, and Variable Pore Diameters (14−23 nm). *J. Am. Chem. Soc.* **2010**, *132*, 4438−4444.

(22) Chen, J. S.; Tan, Y. L.; Li, C. M.; Cheah, Y. L.; Luan, D.; Madhavi, S.; Boey, F. Y. C.; Archer, L. A.; Lou, X. W. Constructing Hierarchical Spheres from Large Ultrathin Anatase TiO_2 Nanosheets with Nearly 100% Exposed (001) Facets for Fast Reversible Lithium Storage. *J. Am. Chem. Soc.* **2010**, *132*, 6124−6130.

(23) Ren, H.; Yu, R.; Wang, J.; Jin, Q.; Yang, M.; Mao, D.; Kisailus, D.; Zhao, H.; Wang, D. Multishelled TiO_2 Hollow Microspheres as Anodes with Superior Reversible Capacity for Lithium Ion Batteries. *Nano Lett.* **2014**, *14*, 6679−6684.

(24) Liu, H.; Li, W.; Shen, D.; Zhao, D.; Wang, G. Graphitic Carbon Conformal Coating of Mesoporous TiO_2 Hollow Spheres for High-Performance Lithium Ion Battery Anodes. *J. Am. Chem. Soc.* **2015**, *137*, 13161−13166.

(25) Yang, Z.-Z.; Wang, H.-Y.; Lu, L.; Wang, C.; Zhong, X.-B.; Wang, J.-G.; Jiang, Q.-C. Hierarchical TiO_2 Spheres as Highly Efficient Polysulfide Host for Lithium-Sulfur Batteries. *Sci. Rep.* **2016**, *6*, 22990.

(26) Froschl, T.; Hormann, U.; Kubiak, P.; Kucerova, G.; Pfanzelt, M.; Weiss, C. K.; Behm, R. J.; Husing, N.; Kaiser, U.; Landfester, K.; Wohlfahrt-Mehrens, M. High Surface Area Crystalline Titanium Dioxide: Potential and Limits in Electrochemical Energy Storage and Catalysis. *Chem. Soc. Rev.* **2012**, *41*, 5313−5360.

(27) Connal, L. A.; Lynd, N. A.; Robb, M. J.; See, K. A.; Jang, S. G.; Spruell, J. M.; Hawker, C. J. Mesostructured Block Copolymer Nanoparticles: Versatile Templates for Hybrid Inorganic/Organic Nanostructures. *Chem. Mater.* **2012**, *24*, 4036−4042.

DOI: 10.1021/acsami.7b03155

(28) Eiden-Assmann, S.; Widoniak, J.; Maret, G. Synthesis and Characterization of Porous and Nonporous Monodisperse Colloidal TiO_2 Particles. *Chem. Mater.* **2004**, *16*, 6−11.

(29) Zhang, Y.; Tan, H.; Li, H.; Liu, Y.-Q.; Kartawidjaja, F. C.; Yang, Z.-C.; Wang, J. Hybrid Titania Microspheres of Novel Superstructures Templated by Block Copolymers. *Chem. Mater.* **2011**, *23*, 2745−2752.

(30) Hong, M. P.; Kim, J. Y.; Vemula, K.; Kim, H. S.; Yoon, K. B. Synthesis of Monodisperse Mesoporous TiO_2 Spheres with Tunable Sizes Between 0.6 and 3.1 μm and Effects of Reaction Temperature, Ti Source Purity, and Type of Alkylamine on Size and Monodispersity. *Chem. Commun.* **2012**, *48*, 4250−4252.

(31) Liu, H.; Grey, C. P. Influence of Particle Size, Cycling Rate and Temperature on the Lithiation Process of Anatase TiO_2. *J. Mater. Chem. A* **2016**, *4*, 6433−6446.

(32) Yang, P.; Zhao, D.; Margolese, D. I.; Chmelka, B. F.; Stucky, G. D. Generalized Syntheses of Large-Pore Mesoporous Metal Oxides with Semicrystalline Frameworks. *Nature* **1998**, *396*, 152−155.

(33) Soler-Illia, G. J. d. A. A.; Louis, A.; Sanchez, C. Synthesis and Characterization of Mesostructured Titania-Based Materials through Evaporation-Induced Self-Assembly. *Chem. Mater.* **2002**, *14*, 750−759.

(34) Fattakhova-Rohlfing, D.; Wark, M.; Brezesinski, T.; Smarsly, B.; Rathouský, J. Highly Organized Mesoporous TiO_2 Films with Controlled Crystallinity: A Li-Insertion Study. *Adv. Funct. Mater.* **2007**, *17*, 123−132.

(35) Lee, J.; Jung, Y. S.; Warren, S. C.; Kamperman, M.; Oh, S. M.; DiSalvo, F. J.; Wiesner, U. Direct Access to Mesoporous Crystalline TiO_2/Carbon Composites with Large and Uniform Pores for Use as Anode Materials in Lithium Ion Batteries. *Macromol. Chem. Phys.* **2011**, *212*, 383−390.

(36) Ren, Y.; Hardwick, L.; Bruce, P. Lithium Intercalation into Mesoporous Anatase with an Ordered 3D Pore Structure. *Angew. Chem., Int. Ed.* **2010**, *49*, 2570−2574.

(37) Kang, E.; Jung, Y. S.; Kim, G.-H.; Chun, J.; Wiesner, U.; Dillon, A. C.; Kim, J. K.; Lee, J. Highly Improved Rate Capability for a Lithium-Ion Battery Nano-$Li_4Ti_5O_{12}$ Negative Electrode via Carbon-Coated Mesoporous Uniform Pores with a Simple Self-Assembly Method. *Adv. Funct. Mater.* **2011**, *21*, 4349−4357.

(38) Jo, C.; Kim, Y.; Hwang, J.; Shim, J.; Chun, J.; Lee, J. Block Copolymer Directed Ordered Mesostructured $TiNb_2O_7$ Multimetallic Oxide Constructed of Nanocrystals as High Power Li-Ion Battery Anodes. *Chem. Mater.* **2014**, *26*, 3508−3514.

(39) Jeon, S.-J.; Yi, G.-R.; Yang, S.-M. Cooperative Assembly of Block Copolymers with Deformable Interfaces: Toward Nanostructured Particles. *Adv. Mater.* **2008**, *20*, 4103−4108.

(40) Deng, R.; Liu, S.; Li, J.; Liao, Y.; Tao, J.; Zhu, J. Mesoporous Block Copolymer Nanoparticles with Tailored Structures by Hydrogen-Bonding-Assisted Self-Assembly. *Adv. Mater.* **2012**, *24*, 1889−1893.

(41) La, Y.; Park, C.; Shin, T. J.; Joo, S. H.; Kang, S.; Kim, K. T. Colloidal Inverse Bicontinuous Cubic Membranes of Block Copolymers with Tunable Surface Functional Groups. *Nat. Chem.* **2014**, *6*, 534−541.

(42) Kim, M. P.; Yi, G.-R. Nanostructured Colloidal Particles by Confined Self-Assembly of Block Copolymers in Evaporative Droplets. *Front. Mater.* **2015**, *2*, 45.

(43) Lee, J.; Christopher Orilall, M.; Warren, S. C.; Kamperman, M.; DiSalvo, F. J.; Wiesner, U. Direct Access to Thermally Stable and Highly Crystalline Mesoporous Transition-Metal Oxides with Uniform Pores. *Nat. Mater.* **2008**, *7*, 222−228.

(44) Stefik, M.; Song, J.; Sai, H.; Guldin, S.; Boldrighini, P.; Orilall, M. C.; Steiner, U.; Gruner, S. M.; Wiesner, U. Ordered Mesoporous Titania from Highly Amphiphilic Block Copolymers: Tuned Solution Conditions Enable Highly Ordered Morphologies and Ultra-Large Mesopores. *J. Mater. Chem. A* **2015**, *3*, 11478−11492.

(45) Wu, Q. L.; Subramanian, N.; Rankin, S. E. Hierarchically Porous Titania Thin Film Prepared by Controlled Phase Separation and Surfactant Templating. *Langmuir* **2011**, *27*, 9557−9566.

(46) Sai, H.; Tan, K. W.; Hur, K.; Asenath-Smith, E.; Hovden, R.; Jiang, Y.; Riccio, M.; Muller, D. A.; Elser, V.; Estroff, L. A.; Gruner, S. M.; Wiesner, U. Hierarchical Porous Polymer Scaffolds from Block Copolymers. *Science* **2013**, *341*, 530−534.

(47) He, D.; Ekere, N. N.; Cai, L. Computer simulation of random packing of unequal particles. *Phys. Rev. E: Stat. Phys., Plasmas, Fluids, Relat. Interdiscip. Top.* **1999**, *60*, 7098−7104.

(48) Brunauer, S.; Emmett, P. H.; Teller, E. Adsorption of Gases in Multimolecular Layers. *J. Am. Chem. Soc.* **1938**, *60*, 309−319.

(49) Barrett, E. P.; Joyner, L. G.; Halenda, P. P. The Determination of Pore Volume and Area Distributions in Porous Substances. I. Computations from Nitrogen Isotherms. *J. Am. Chem. Soc.* **1951**, *73*, 373−380.

(50) Guldin, S.; Huttner, S.; Tiwana, P.; Orilall, M. C.; Ulgut, B.; Stefik, M.; Docampo, P.; Kolle, M.; Divitini, G.; Ducati, C.; Redfern, S. A. T.; Snaith, H. J.; Wiesner, U.; Eder, D.; Steiner, U. Improved Conductivity in Dye-Sensitised Solar Cells Through Block-Copolymer Confined TiO_2 Crystallisation. *Energy Environ. Sci.* **2011**, *4*, 225−233.

(51) Patterson, A. L. The Scherrer Formula for X-Ray Particle Size Determination. *Phys. Rev.* **1939**, *56*, 978−982.

(52) Czanderna, A. W.; Rao, C. N. R.; Honig, J. M. The Anatase-Rutile Transition. Part 1.-Kinetics of the Transformation of Pure Anatase. *Trans. Faraday Soc.* **1958**, *54*, 1069−1073.

(53) Patra, S.; Davoisne, C.; Bouyanfif, H.; Foix, D.; Sauvage, F. Phase Stability Frustration on Ultra-Nanosized Anatase TiO_2. *Sci. Rep.* **2015**, *5*, 10928.

(54) Hanaor, D. A. H.; Sorrell, C. C. Review of the anatase to rutile phase transformation. *J. Mater. Sci.* **2011**, *46*, 855−874.

(55) Wagemaker, M.; Borghols, W. J. H.; Mulder, F. M. Large Impact of Particle Size on Insertion Reactions. A Case for Anatase Li_xTiO_2. *J. Am. Chem. Soc.* **2007**, *129*, 4323−4327.

(56) Wang, J.; Polleux, J.; Lim, J.; Dunn, B. Pseudocapacitive Contributions to Electrochemical Energy Storage in TiO_2 (Anatase) Nanoparticles. *J. Phys. Chem. C* **2007**, *111*, 14925−14931.

(57) Brezesinski, T.; Wang, J.; Polleux, J.; Dunn, B.; Tolbert, S. H. Templated Nanocrystal-Based Porous TiO_2 Films for Next-Generation Electrochemical Capacitors. *J. Am. Chem. Soc.* **2009**, *131*, 1802−1809.

(58) Borghols, W. J. H.; Lützenkirchen-Hecht, D.; Haake, U.; Chan, W.; Lafont, U.; Kelder, E. M.; van Eck, E. R. H.; Kentgens, A. P. M.; Mulder, F. M.; Wagemaker, M. Lithium Storage in Amorphous TiO_2 Nanoparticles. *J. Electrochem. Soc.* **2010**, *157*, A582−A588.

(59) Lim, J.; Um, J. H.; Lee, K. J.; Yu, S.-H.; Kim, Y.-J.; Sung, Y.-E.; Lee, J.-K. Simple Size Control of TiO_2 Nanoparticles and their Electrochemical Performance: Emphasizing the Contribution of the Surface Area to Lithium Storage at High-Rates. *Nanoscale* **2016**, *8*, 5688−5695.

(60) Belak, A. A.; Wang, Y.; Van der Ven, A. Kinetics of Anatase Electrodes: The Role of Ordering, Anisotropy, and Shape Memory Effects. *Chem. Mater.* **2012**, *24*, 2894−2898.

(61) Dylla, A. G.; Henkelman, G.; Stevenson, K. J. Lithium Insertion in Nanostructured TiO_2(B) Architectures. *Acc. Chem. Res.* **2013**, *46*, 1104−1112.

(62) Zukalová, M.; Kalbáč, M.; Kavan, L.; Exnar, I.; Graetzel, M. Pseudocapacitive Lithium Storage in TiO_2(B). *Chem. Mater.* **2005**, *17*, 1248−1255.

(63) Richter, J. H.; Henningsson, A.; Karlsson, P. G.; Andersson, M. P.; Uvdal, P.; Siegbahn, H.; Sandell, A. Electronic Structure of Lithium-Doped Anatase TiO_2 Prepared in Ultrahigh Vacuum. *Phys. Rev. B: Condens. Matter Mater. Phys.* **2005**, *71*, 235418.

(64) Borghols, W. J. H.; Lutzenkirchen-Hecht, D.; Haake, U.; van Eck, E. R. H.; Mulder, F. M.; Wagemaker, M. The Electronic Structure and Ionic Diffusion of Nanoscale $LiTiO_2$ Anatase. *Phys. Chem. Chem. Phys.* **2009**, *11*, 5742−5748.

(65) Shin, J.-Y.; Joo, J. H.; Samuelis, D.; Maier, J. Oxygen-Deficient $TiO_{2-\delta}$ Nanoparticles via Hydrogen Reduction for High Rate Capability Lithium Batteries. *Chem. Mater.* **2012**, *24*, 543−551.